RSC Advances

ROYAL SOCIETY OF CHEMISTRY

PAPER

View Article Online
View Journal | View Issue

Cite this: *RSC Adv.*, 2024, **14**, 18777

Investigation on structure and photoluminescence properties of Ho^{3+} doped $Ca_3(VO_4)_2$ phosphors for luminescent devices

Vijay Singh, *[a] Aadil Ahmad Bhat,[a] M. Radha,[b] M. Seshadri,[c] Sooraj H. Nandyala[d] and Ji Bong Joo[a]

This study focuses on the synthesis and characterization of Ho^{3+} doped $Ca_3(VO_4)_2$ phosphor for potential application in solid-state lighting technology. A citrate-based sol–gel process is optimized to achieve sheet-like morphologies in the phosphor material. The investigation reveals UV absorption at 371 nm, indicating a band gap of 3.28 eV. Emission transitions at (506, 541, and 651) nm are observed when excited at 451 nm, with an optimal Ho^{3+} concentration of 0.05 mol resulting in robust green emission at 541 nm. The concentration quenching in $Ca_3(VO_4)_2$:xHo^{3+} phosphors is discussed in detail with Blesse's and Dexter's models. The concentration quenching effect found in the studied samples is due to the dipole–dipole interactions. Judd–Ofelt intensity parameters were calculated from the excitation bands, and for Ω_2, Ω_4, and Ω_6 are (0.16, 0.17, and 0.36) $\times$ 10^{-20} cm^2, respectively. The emission properties for the ($^5S_2$ + $^5F_4$) $\rightarrow$ $^5I_8$ and $^5F_5$ $\rightarrow$ $^5I_8$ transitions are also estimated with *J*–*O* parameters. The higher magnitude of branching ratios (83%) and emission cross-sections (1.6 $\times$ 10^{-21} cm^2) suggest that the $Ca_3(VO_4)_2$:0.05Ho^{3+} phosphor materials may be suitable for efficient green-emitting device applications. The CIE coordinates confirm the potential of Ho^{3+}-doped phosphors for green emissions, making them suitable for solid-state lighting and display technology.

Received 29th April 2024
Accepted 30th May 2024

DOI: 10.1039/d4ra03178d

rsc.li/rsc-advances

1. Introduction

Phosphors play a pivotal role in advancing various lighting and display technologies, with particular importance in developing efficient white light-emitting diodes (w-LEDs) and displays.[1–4] The pursuit of ideal phosphor materials has been driven by the desire to efficiently generate a broad spectrum of colors, particularly in converting ultraviolet (UV) or blue light, which are common excitation sources, into visible light.[5,6] This quest has led to extensive research in the field of phosphor materials, spanning a variety of chemical composition and structural characteristics.[7,8] Among the diverse classes of phosphor materials, vanadate compounds have garnered considerable attention, and one standout candidate in this category is calcium orthovanadate, denoted as $Ca_3(VO_4)_2$, which has piqued the interest of researchers and material scientists due to its unique luminescent properties.[9,10] The choice of vanadate compounds is well-founded, as they offer several advantages. They exhibit tunable emission characteristics; hence the color and intensity of emitted light can be tailored for specific applications.[11–13] This tunability is a crucial feature for creating phosphors that can complement the spectral sensitivity of human vision, resulting in optimal lighting and display quality. $Ca_3(VO_4)_2$, a type of vanadate, has a crystalline structure that, when doped with certain rare-earth ions, can be customized to emit light in the visible spectrum.[14] This feature makes $Ca_3(VO_4)_2$ a compelling option for requiring green emissions, such as in w-LEDs and display technologies.[15] The flexibility of $Ca_3(VO_4)_2$ based phosphors stems from their adjustable emission properties, enabling the creation of materials that emit light in a controlled and effective manner. The development of white light-emitting diodes (LEDs) depends heavily on green-emitting phosphors. Among luminous activators, Tb^{3+} ions are renowned for their excellent quantum yield, radiation purity, and stability.[16,17] To study green luminescence, Tb^{3+} ions have recently been added to host materials, such as BiOCl and $SrAl_2O_4$.[18,19] The $4f^8$–$4f^75d^1$ transition is responsible for the wide excitation properties that Tb^{3+} ions display in the (220–300) nm region. Surprisingly, isolated VO_4^{3-} moieties are also absorbed in this excitation range, possibly serving as Tb^{3+} ion sensitizers. Kuz'micheva *et al.* demonstrate the spectral-luminescent properties in Tm-doped $Ca_3(VO_4)_2$.[20] Voronina *et al.* describe the yellow emission in Mn-doped $Ca_3(VO_4)_2$,[21] while

[a]*Department of Chemical Engineering, Konkuk University, Seoul, 05029, Republic of Korea. E-mail: vijayjiin2006@yahoo.com*

[b]*Department of Physics, Institute of Aeronautical Engineering (IARE), Hyderabad, 500043, India*

[c]*Department of Physics, Koneru Lakshmaiah Education Foundation, Hyderabad, 500043, India*

[d]*School of Metallurgy and Materials, University of Birmingham, Edgbaston, Birmingham, B15 2TT, UK*

Kuz'micheva *et al.* show the presence of both Mn^{2+} and Mn^{3+} in manganese-doped $Ca_3(VO_4)_2$,[22] Chen *et al.* describe the strong absorption at the visible wavelength in Cr-doped $Ca_3(VO_4)_2$,[13] and Ivleva *et al.* report the optical homogeneity in Tm^{3+}/Ho^{3+} co-doped $Ca_3(VO_4)_2$.[23]

In recent years, the focus of research has extended to the doping of $Ca_3(VO_4)_2$ with various rare-earth ions, including trivalent holmium (Ho^{3+}). Incorporating Ho^{3+} ions into the crystal lattice of $Ca_3(VO_4)_2$ has shown promise in generating strong green emissions. This is of great significance in the context of w-LEDs, where achieving a balanced and vibrant white light output depends on the efficient emission of various colors, including green. Vanadate phosphors may be synthesized using a variety of procedures that include co-precipitation,[24] solid-state reaction,[25] hydrothermal synthesis,[26,27] combustion synthesis,[28] and sol–gel approaches.[29] The capacity to obtain phosphors in phase-pure form is critical for fundamental scientific research, as well as practical applications. In this context, the sol–gel methodology used in this work provides a more convenient path than typical solid-state procedures.[30] Traditional procedures require extended preheating and high-temperature sintering, whereas the sol–gel process is a gentler and more efficient alternative. In this investigation, the sol–gel method has been adopted to prepare $Ca_3(VO_4)_2$:Ho^{3+} phosphors. This study investigates $Ca_3(VO_4)_2$:Ho^{3+} phosphors for use as green emitters in solid-state lighting. It examines their crystal structure, morphology, and photoluminescent properties to determine the optimal Ho^{3+} concentration for strong green emissions, showcasing their potential for high-quality green light output.

2. Material synthesis

The sol–gel method for the synthesis of $Ca_3(VO_4)_2$:xHo^{3+} phosphors is a well-controlled and accurately designed process. Each step, from reagent selection to the final heat treatment, plays a critical role in determining the composition, structure, and properties of the phosphor material. The success of this method relies on the precise control of reaction conditions, temperature, and time to achieve the desired outcome, making it suitable for producing specialized materials with tailored characteristics. A suitable amount of initial reagents, such as $Ca(NO_3)_2 \cdot 4H_2O$, NH_4VO_3, $Ho(NO_3)_3 \cdot 6H_2O$, and citric acid (in molar ratio 2 : 1 with metal ion), are mixed in a 150 mL glass beaker with 10 mL of deionized water. This step is key, as it initiates the formation of a sol, which is a colloidal suspension of solid particles in a liquid. The mixture is agitated at 500 rpm for up to 1 hour. During this time, the reagents react, and a yellow liquified solution is formed, ensuring a homogenous product is formed. Citric acid plays a key role in this process as a chelating agent, helping to control the gel formation. After stirring for one hour, the solution is transferred into the oven at 110 °C overnight. This step is important for removing the liquid component and forming a gel. The solution gradually transforms into a gel, which is a three-dimensional network of solid particles held within the liquid medium. The choice of 110 °C temperature and the duration of heating are crucial parameters for controlling the gel formation process. The dry gels obtained from the previous step are sintered at 400 °C for 120 min in the presence of air in a muffle furnace. The specific sintering temperature and duration are carefully selected to ensure that the desired phase is obtained. The last step involves further heating the resultant black powder samples in air at a higher temperature of 800 °C for 2 h in a muffle furnace. This additional heat treatment is likely to optimize the phosphor's properties. It could be necessary to enhance its luminescent characteristics and ensure the formation of the desired crystal structure. A series of $Ca_3(VO_4)_2$:xHo^{3+} ($0.01 \leq x \leq 0.11$) phosphors were synthesized by this approach to understand the impact of Ho^{3+} on the crystal lattice of $Ca_3(VO_4)_2$.

X-ray diffraction (XRD) analysis of the powders was conducted by diffractometry (RIGAKU, Miniflex-II). CuKα radiation (with $\lambda = 1.5406$ Å) was employed as the X-ray source. The patterns were collected at a fixed 5° min^{-1} scan rate ranging 2θ = (10 to 50)°. The morphology study was performed using an S-3400 (Hitachi, Japan) SEM. A Cary 5000, UV-vis instrument was used to record the UV-vis reflectance spectra. Luminescence studies were conducted *via* fluorescence spectrometry (Shimadzu, RF-5301PC), with an attached xenon flash lamp as the excitation source.

3. Results and discussion

3.1 X-ray diffraction (XRD)

The structure of $Ca_3(VO_4)_2$:Ho^{3+} phosphors is crucial for customizing their properties for various applications, especially in luminescent devices. The X-ray diffraction patterns for holmium-doped calcium orthovanadate phosphors lie in a (10 to 50)° range, as shown in Fig. 1. The XRD peaks observed match well with the JCPDS card no. 46-0756, indicating the formation of $Ca_3(VO_4)_2$:Ho^{3+} phosphor. As the percentage of dopant within $Ca_3(VO_4)_2$ is increased, secondary peaks emerge in XRD patterns, indicative of secondary phase (marked by the symbol*) formation beyond optimal concentrations. The secondary peak most likely belongs to the CaV_2O_5 material, which is formed when Ho^{3+} is incorporated.[12] This XRD peak most likely belongs to CaV_2O_5, which is the most prominent peak in JCPDS card no. 30-0286. With increasing Ho^{3+} ion concentration, the intensity of the secondary peak continuously increases. However, XRD did not reveal the presence of a dopant peak as an impurity. The successful incorporation of Ho^{3+} ions into the $Ca_3(VO_4)_2$ host lattice is indicated by their substitution for Ca^{2+} ions, facilitated by their comparable ionic radius of Ho^{3+} (1.01 Å) and Ca^{2+} (1.12 Å) ions.[20,23,31] Whereas the V^{5+} ionic radius is about 0.35 Å, which is smaller than the Ho^{3+} and Ca^{2+} ions, thus V^{5+} ions can't be facilitated as an interstitial atom for Ho^{3+} ions. Chauhan *et al.* have reported that in the host structure $Ca_3(VO_4)_2$, the Sm^{3+} ion can replace the Ca^{2+} site.[32] This substitution leads to a noticeable shift in the XRD patterns, with the shift towards higher angles. The difference in ionic radii between Sm^{3+} and Ca^{2+} ions accounts for this shift. Specifically, the larger size of the Sm^{3+} ion, compared to Ca^{2+}, disrupts the regular lattice arrangement, resulting in alterations in the diffraction pattern.[32] Ivleva *et al.* also reported the substitution

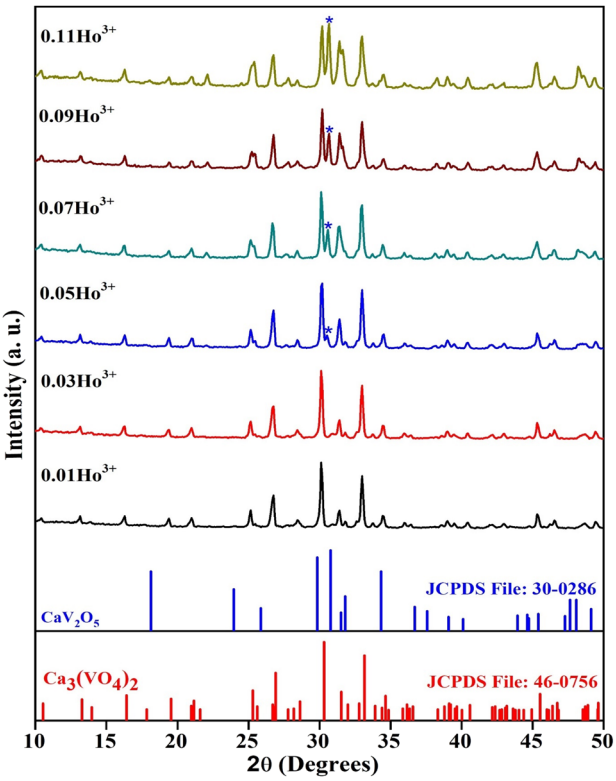

Fig. 1 XRD patterns of $Ca_3(VO_4)_2$:xHo^{3+} phosphors along with standard JCPDS cards data of $Ca_3(VO_4)_2$ and CaV_2O_5.

of rare earth elements (Tm + Ho) into the Ca^{2+} site of $Ca_3(VO_4)_2$.[23] Li *et al.* found that Eu^{3+} ions were successfully substituted for Ca^{2+} ions in the rhombohedral phase of $Ca_3(VO_4)_2$. This substitution was possible due to the similar ionic radii of Eu^{3+} and Ca^{2+}.[33] Kuz'micheva *et al.* propose that Mn^{5+} can replace V^{5+} ions in $Ca_3(VO_4)_2$, a substitution supported by previous research.[22] Based on the results, Ho^{3+} ions could potentially replace Ca^{2+} ions in the crystal lattice of $Ca_3(VO_4)_2$, similar to Eu^{3+} ions. The XRD pattern justifies the presence of a hexagonal phase with the space symmetry of *R3c*. The average crystallite size is calculated using the Scherrer equation:[34]

$$D = 0.9\lambda/\beta\cos\theta \quad (1)$$

All the samples exhibit an average crystallite size of <50 nm, which provides evidence for the use of these materials in nanomaterial technology. The crystallite size can affect the peak shape, intensity, and broadening in XRD patterns. These changes can impact the ability to identify the phase of a nanomaterial. The crystallite size can influence the physical and chemical properties of nanomaterials, including their mechanical, electrical, and catalytic properties, making it a critical parameter to consider in nanoscience and materials research. It has been observed from Table 1 that all the samples exhibit uniform crystallite size, but the sample with optimal concentration of Ho^{3+} shows a slight decrease in crystallite size, because the initial introduction of dopants might have a more

Table 1 Crystallite size and lattice strain of all samples

S. no.	Material composition	Crystallite size (nm)	Lattice strain
1	$Ca_3(VO_4)_2$:0.01Ho^{3+}	42.98	0.0032
2	$Ca_3(VO_4)_2$:0.03Ho^{3+}	42.98	0.0032
3	$Ca_3(VO_4)_2$:0.05Ho^{3+}	40.93	0.0034
4	$Ca_3(VO_4)_2$:0.07Ho^{3+}	42.94	0.0034
5	$Ca_3(VO_4)_2$:0.09Ho^{3+}	42.98	0.0032
6	$Ca_3(VO_4)_2$:0.11Ho^{3+}	42.98	0.0032

pronounced effect on crystallite size, as they have a significant impact on the crystal structure. As the dopant concentration increases, the effects may saturate or reach a maximum, and further doping does not have as significant an impact on the crystallite size. Fig. 2 shows the structure of the $Ca_3(VO_4)_2$ and Ho^{3+}-doped $Ca_3(VO_4)_2$ crystal structures.

3.2 Scanning electron microscopy (SEM)

Morphological analysis can provide valuable insights into the physical properties and structure of $Ca_3(VO_4)_2$, which is important for understanding its behavior and applications in various fields, such as materials science, chemistry, and solid-state physics. Fig. 3a represents the SEM micrographs of the $Ca_3(VO_4)_2$:0.05Ho^{3+} phosphor. The morphology depicts the irregular sheet-like morphology formed throughout the whole sample and shows that there is no regularity in the particle size of the $Ca_3(VO_4)_2$:0.05Ho^{3+} phosphor. The formation of irregular sheet-like morphology in materials like $Ca_3(VO_4)_2$ can be influenced by various factors that include chemical composition, crystal structure, synthesis conditions, and growth mechanisms.[35] The initial nucleation of crystals and their subsequent growth can lead to the formation of sheet-like structures if the growth rate in one dimension is much faster than in the others. This can result in the development of thin, plate-like crystals or sheets. Fig. 3b (enlarged view of zone (a′)) represents a magnified version of the $Ca_3(VO_4)_2$:0.05Ho^{3+} phosphor material, in which both small and large particles can be observed. Note also that a few pores are present in the particles, which is due to the ejection of large amounts of hot gases while heating the xerogels.[36] The presence of such pores in xerogels is not unusual and can affect the physical properties of the material. The size and distribution of the pores can vary depending on factors like the gel preparation method, type of solvent used, heating conditions, and gel composition.[37] In some cases, these pores may be considered a desirable feature, such as in applications where a high surface area or improved adsorption properties are required.[38] The control of pore size and distribution in xerogels is an important aspect of their synthesis, and adjusting the drying conditions and gel composition can be used to tailor the resulting porosity to meet specific application requirements.[39] The presence of certain additives, impurities, or surfactants in the synthesis process can influence crystal growth and morphology. These substances can affect the rate of growth along different crystallographic directions, potentially leading to the formation of sheets.

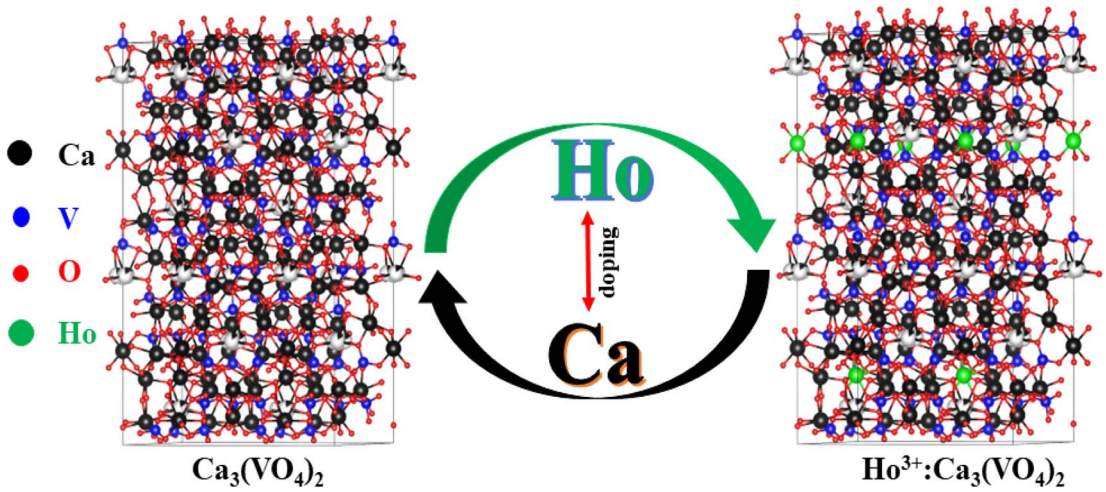

Fig. 2 General view of $Ca_3(VO_4)_2$ and Ho^{3+} doped $Ca_3(VO_4)_2$ crystal structure.

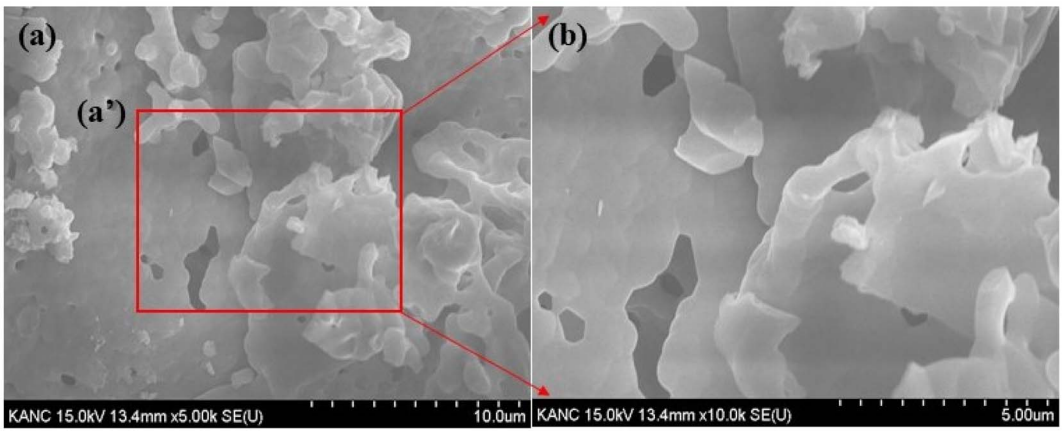

Fig. 3 SEM images of $Ca_3(VO_4)_2$:0.05Ho^{3+} phosphor.

3.3 UV-vis reflectance spectroscopy

The reflection peaks of the synthesized $Ca_3(VO_4)_2$:0.05Ho^{3+} phosphor serve as distinctive markers of energy transitions in Ho^{3+} ions. They offer a comprehensive perspective on the rich energy level structure of the 4f electron shell, and open exciting possibilities for exploiting these materials in advanced photonic and optoelectronic technologies. The observed reflection peaks in the $Ca_3(VO_4)_2$:0.05Ho^{3+}, spanning a broad wavelength ranging (200 to 2000) nm, provide valuable insights into the optical properties and energy level structure of the Ho^{3+} ions doped into the host material. Fig. 4a shows the diffuse reflectance spectrum of the $Ca_3(VO_4)_2$:0.05Ho^{3+} phosphor. The distinctive peaks, appearing at approximately (420, 456, 487, 544, and 650) nm, correspond to energy absorption processes from the $^5I_8$ ground state of the Ho^{3+} ions to various excited states within the 4f electron shell.[40,41] These transitions are associated with the $4f^{10}$–$4f^{10}$ electronic configuration of Ho^{3+} ions and carry significant implications for the study of rare earth-doped materials and their applications in optoelectronics and photonics. The absorption peak at around 420 nm is attributed to the $^5G_5$ transition. This phenomenon involves the promotion of Ho^{3+} ions from their ground state ($^5I_8$) to the excited $^5G_5$ state. This transition underscores the specificity of the electronic transitions within Ho^{3+} ions, while also serving as a key reference point for characterizing the material's optical behavior. The reflection peak at 456 nm is indicative of a more complex transition. At this wavelength, Ho^{3+} ions are undergoing simultaneous excitation to two different states, namely, the $^5G_6$ and $^5F_1$ states. This suggests that the absorption of energy leads to changes in the electron configuration of Ho^{3+} ions, including both $^5G_6$ and $^5F_1$ transitions. The peak at 487 nm corresponds to the $^5F_3$ transition, which signifies the absorption of energy, enabling Ho^{3+} ions to transition from their ground state to the excited $^5F_3$ state. This transition adds to the spectrum of energy levels accessible to Ho^{3+} ions and is a crucial factor in understanding their optical characteristics. At 544 nm, the spectral feature is associated with the simultaneous excitation of two states, $^5F_4$ and $^5S_2$. This points to the versatility of the electronic transitions within Ho^{3+} ions, allowing them to be promoted to multiple excited states with distinct energy levels. This transition, reflecting the rich energy level structure

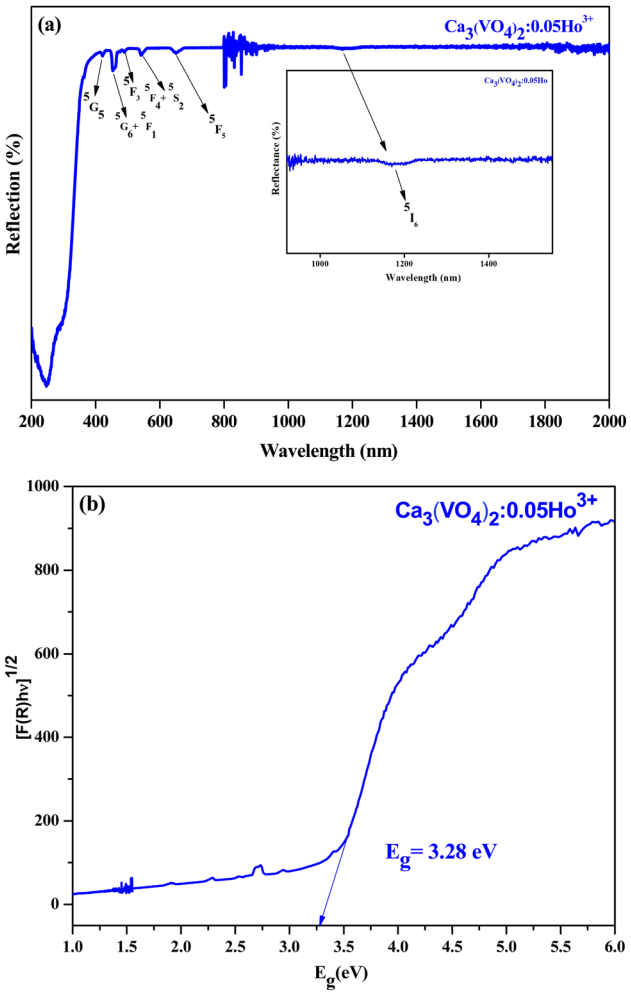

Fig. 4 (a) UV-vis spectrum of $Ca_3(VO_4)_2$:0.05Ho^{3+} phosphor. (b) Band gap of $Ca_3(VO_4)_2$:0.05Ho^{3+} phosphor.

of the 4f shell, holds the key to the optical behavior of the material. The peak at 650 nm corresponds to the $^5F_5$ transition, signifying the absorption of energy that leads to the transition of Ho^{3+} ions from their ground state to the $^5F_5$ excited state. This transition offers further evidence of the intricate energy level structure present in the 4f electron shell of Ho^{3+} ions. The additional peak at 1200 nm is associated with the $^5I_6$ transition. This transition entails the promotion of Ho^{3+} ions from their ground state, $^5I_8$, to the $^5I_6$ excited state.[41] The observation of these well-defined reflection peaks both allows for the precise identification of Ho^{3+} ion transitions and contributes to our understanding of the optical properties of rare earth doped materials. These findings are of significant relevance to the development of novel photonic devices, such as lasers and amplifiers, and to the design of phosphors with tailored luminescent properties.

The band gap estimation using the Kubelka–Munk equation and diffused reflectance spectroscopy (DRS) provides valuable information about the material's semiconducting properties and its suitability for specific optical and electronic applications.[42] The determination of the band gap of the $Ca_3(VO_4)_2$ doped with Ho^{3+} at a concentration of 0.05 using the Kubelka–Munk equation is a significant finding of this study. Fig. 4b shows the variation of plots of $(F(R)hv)^{1/2}$ as a function of E_g (eV). The obtained direct band gap value of 3.28 eV carries important implications for the optical and electronic properties of the doped material. The incorporation of Ho ions into the material introduces energy levels associated with the 4f electron shell of Ho^{3+} ions. The specific electronic transitions within the 4f shell contribute to the observed band gap and influence the material's optical properties. The presence of rare earth ions like Ho is known to introduce complex energy-level structures, offering opportunities for tailored design in photonics and luminescence. The direct band gap value of 3.28 eV is of considerable significance and indicates that the doped material is a wide-band gap semiconductor. Wide-band gap materials typically have band gaps greater than 3 eV and are known for their suitability in applications where higher-energy photons, such as ultraviolet and blue light, are involved.[43] This means that the material can absorb and emit light in the UV and visible regions of the electromagnetic spectrum.

3.4 Photoluminescence spectroscopy and radiative properties

Fig. 5a shows the holmium ion concentration-based excitation spectra of the $Ca_3(VO_4)_2$ phosphors. The excitation spectra were observed at 545 nm, and exhibited some broad, double, and sharp bands in the UV and visible regions. In the UV region, the transitions are assigned as follows from the ground state: $^5I_8$ to various excited states, $^3H_6$ (361 nm), and $^5G_4$ (382 nm). Similarly, in the visible region, $^5G_5$ (420 nm), $^5F_1$ (451 nm), $^5G_6$ (458 nm) $^3K_8$ (469 nm), $^5F_2$ (476 nm), and $^5F_3$ (500 nm).[44] Of the five visible bands, a sharp and highly intense band was noticed at 451 nm ($^5I_8 \rightarrow {}^5F_1$); therefore, the transition wavelength (451 nm) was chosen for the investigation of visible emission spectra for various doping of Ho^{3+} in the calcium orthovanadate $Ca_3(VO_4)_2$ phosphors. The emission spectra from various doping concentrations of Ho^{3+} in the calcium orthovanadate $Ca_3(VO_4)_2$ phosphors were computed in the (500–750) nm range at a 451 nm excitation wavelength and are described in Fig. 5b. The spectra display three emission peaks, among them, a very weak peak around 506 nm, which is assigned to $^5F_3 \rightarrow {}^5I_8$. There is another short peak in the red region at 650 nm ($^5F_5 \rightarrow {}^5I_8$).[45–47] A third intense emission is in the green region at 545 nm and relates to the ($^5S_2 + {}^5F_4$) $\rightarrow {}^5I_8$ transition.[48] When excited at 451 nm, a non-radiative decay was observed from $^5G_5$ to ($^5S_2 + {}^5F_4$) and $^5F_5$ levels, because of the tightly spaced higher energy levels. From these excitation levels, de-excitation leads to green emission. It has been observed that as the concentration of Ho^{3+} ion rises within the range (0.01 to 0.05) mol, the emission transition intensities exhibit a notable increase. However, when the concentration exceeds 0.05 mol, a critical turning point occurs, leading to a diminishing of emission intensities. This phenomenon is attributed to concentration quenching. Fig. 6 depicts the variation of emission intensity of the $^5F_3 \rightarrow {}^5I_8$ transition as a function of the Ho^{3+} ions concentration. The observed luminescence quenching indicates that interactions and energy transfers occur among Ho^{3+} ions within various sites

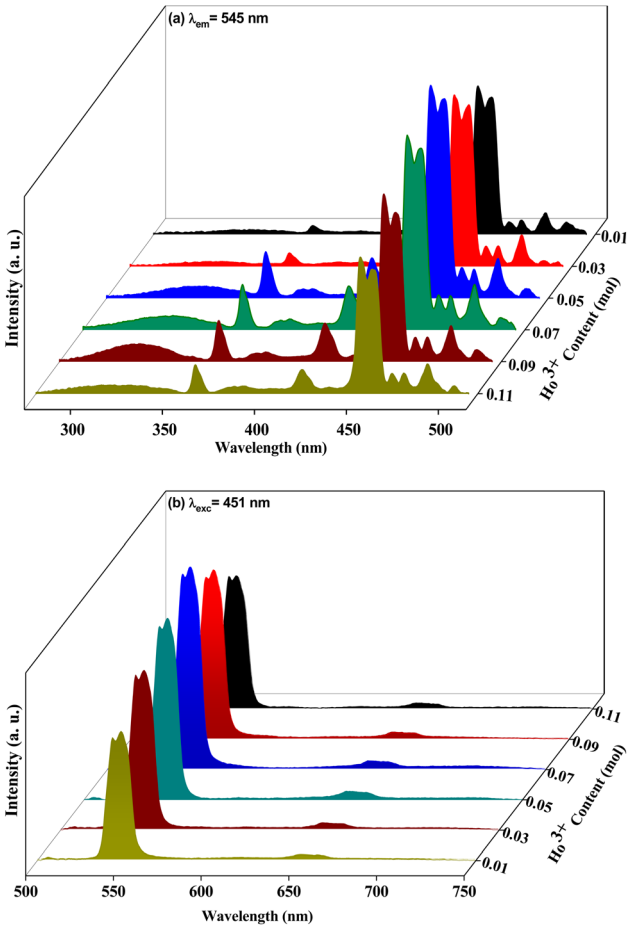

Fig. 5 Photoluminescence spectra of the $Ca_3(VO_4)_2$:xHo^{3+} phosphor (a) excitation spectrum of $Ca_3(VO_4)_2$:xHo^{3+} (λ_{em} = 545 nm) and (b) emission spectrum of $Ca_3(VO_4)_2$:xHo^{3+} (λ_{exc} = 451 nm).

of the lattice, primarily through non-radiative relaxation processes. Normally, the excitation photon energy greatly depends on the concentration of Ho^{3+} ions and is exchanged between Ho–Ho ions. The increase in Ho^{3+} ion concentration leads to a shorter distance between the Ho–Ho ions, which promotes the non-radiative transfer of energy between them. Hence this leads to luminescence quenching, which often influences the luminescence efficiency of the Ho^{3+} phosphors. Fig. 7 presents the possible cross-relaxations in the Ho^{3+} doped phosphor with excitation and emission transitions. According to Blasse's model,[49] the critical distance between Ho–Ho for energy transfer in the $Ca_3(VO_4)_2$:$0.05Ho^{3+}$ phosphor is estimated from the following expression:

$$R_c \approx 2\left[\frac{3V}{4\pi x_C N}\right]^{1/3} \quad (2)$$

in which, V is the volume of the unit cell, x_C is the optimal ion concentration, and N is the number of Z ions per unit cell. In the present study, the critical distance R_c of 11.75 Å is obtained using the parameters, V = 3846.50 Å^3,[12] N = 21, and X_c = 0.05. The obtained R_c indicates that the non-radiative transfer of energy due to the resonance transfer between the Ho–Ho ions is

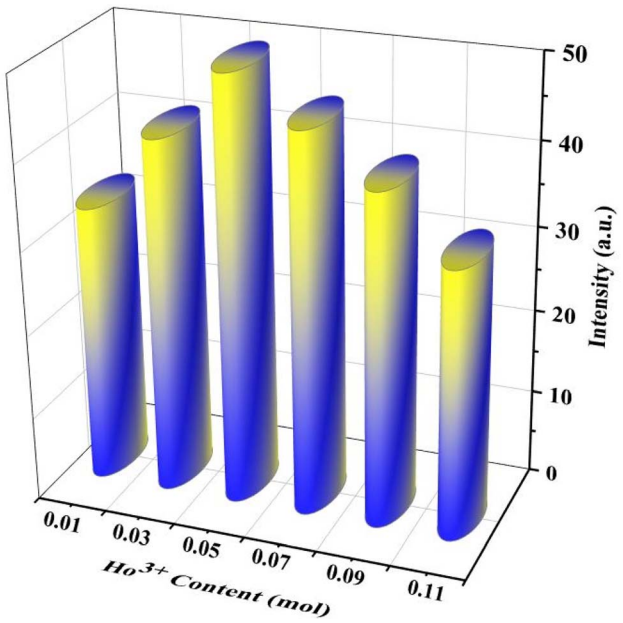

Fig. 6 Variation in the emission intensity of strong emission (545 nm) as a function of Ho^{3+} concentration.

efficient from the electric multipole–multipole interactions. On the other hand, the exchange interaction is inefficient (the multipole–multipole interaction is efficient) between Ho–Ho ions, since R_c is much greater than 5 Å.[49]

It is known that dipole–dipole (d–d), dipole–quadrupole (d–q), and quadrupole–quadrupole (q–q) interactions are responsible for the transfer of energy between Ho–Ho ions, and therefore it is possible to identify the type of interaction with the measured emission intensity and ion concentration in the present study using the following formula:[50]

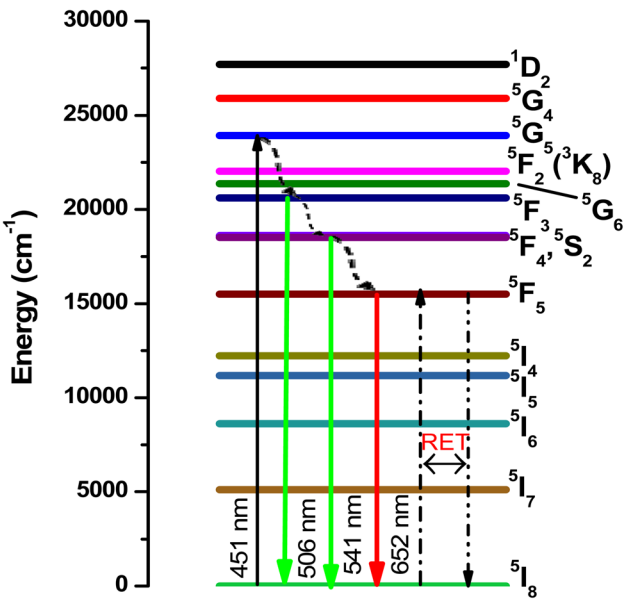

Fig. 7 Schematic energy level diagram for Ho^{3+} ions with possible radiative and non-radiative transitions with possible cross-relaxation.

$$\frac{I}{x} = K\left\{1 + \beta(x)^{Q/3}\right\}^{-1} \quad (3)$$

where, K and β are constants, I is the intensity of emission at 506 nm, x is the Ho^{3+} ion concentration, and Q indicates the multipolar character, where $Q = 6$ for dipole–dipole (d–d), $Q = 8$ for dipole–quadrupole (d–q), and $Q = 10$ for quadrupole–quadrupole (q–q) interactions, respectively. The Q can be obtained from the plot of $\log(I/x)$ as a function of $\log(x)$ at 541 nm ($\lambda_{exc} = 451$ nm), as shown in Fig. 8. The variation between the $\log(I/x)$ *vs.* $\log(x)$ is linear, while the slope $(-Q/3)$ is found to be -1.02. The obtained Q is 3.06, which is closer to 6, indicating that the resonance transfer of energy mechanism for the $Ca_3(VO_4)_2$:Ho^{3+} phosphor is dipole–dipole interactions. Therefore, it can be inferred that the optimum concentration of Ho^{3+} ions in the calcium orthovanadate ($Ca_3(VO_4)_2$) phosphors is around 0.05 mol.

According to ref. 51–54, using the photoluminescence excitation (PLE) spectrum of $Ca_3(VO_4)_2$:$0.05Ho^{3+}$ phosphor sample, the radiative properties, such as the radiative transition probabilities (A_R), branching ratios (β), and radiative lifetimes (τ_R) for certain excited states of Ho^{3+}, are estimated by applying the Judd–Ofelt theory.[55,56] Based on the Judd–Ofelt (J–O) theory, the

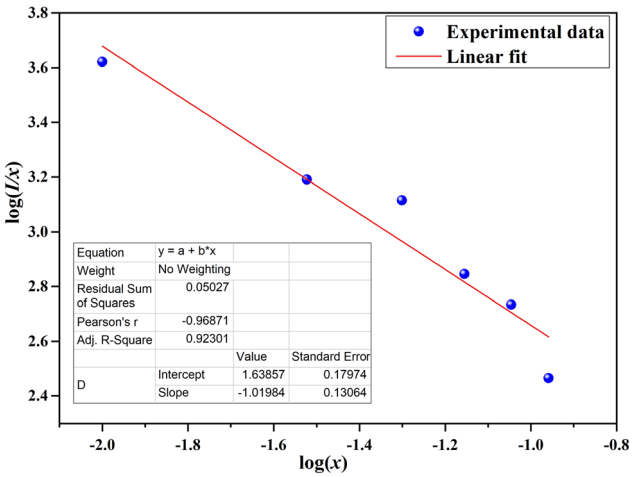

Fig. 8 Plot of $\log(I/x)$ as a function of $\log(x)$ of the $Ca_3(VO_4)_2$:$0.05Ho^{3+}$ phosphor.

J–O intensity parameters Ω_λ ($\lambda = 2$, 4, and 6) can be determined from the PLE spectrum by evaluating the measured and calculated spectral line strengths of excited 4f–4f electronic transitions using the least-square fit method. The relative expressions and theories for the measured and calculated spectral line strengths, radiative transition probabilities (A_R), branching ratios (β), and radiative lifetimes (τ_R) are available elsewhere; therefore, we are presenting only the significant results. Table 2 shows the spectral line strengths for the observed excitation bands and Judd–Ofelt intensity parameters. The Ω_λ parameters are important for the study of the local structure and bonding in the vicinity of rare earth ions. Peacock[57] indicated that the Ω_2 parameter is sensitive to both asymmetry and covalency at rare earth sites, while Oomen *et al.*[58] observed that the rigidity or long-range effects of hosts were responsible for changes in Ω_4 and Ω_6. The obtained values of Ω_2, Ω_4, and Ω_6 for the $Ca_3(VO_4)_2$:$0.05Ho^{3+}$ phosphor is (0.16, 0.17, and 0.36) $\times 10^{-20}$ cm^2, respectively. The magnitude of Ω_2 is comparable to that of the $SrZrO_3$ (ref. 54) and $Lu_3Al_5O_{12}$ (ref. 59) phosphors and has a higher covalency than the YAG[60] host matrix.

Using Ω_λ parameters, the emission properties, such as the radiative transition probabilities (A_{rad}), radiative lifetimes (τ_{rad}), branching ratios (β), and emission cross-sections (σ_{emi}), for the observed emission transitions, $^5S_2 + {}^5F_4 \rightarrow {}^5I_8$ and $^5F_5 \rightarrow {}^5I_8$, are calculated, and are reported in Table 3. The stimulated emission cross-section is an important feature for low threshold and high gain applications. The stimulated emission cross-section (σ_{emi}) can be determined using the formula:[61]

$$\sigma_{emi}(\lambda) = \frac{\lambda_p{}^4}{8\pi c n^2 \Delta\lambda_{eff}} \cdot A_{rad} \quad (4)$$

where, λ is the emission peak wavelength, $\Delta\lambda_{eff}$ is the effective line width, c is the velocity of light, n is the refractive index, and A_{rad} is the radiative transition probability of related emission transition that is calculated using the Judd–Ofelt theory. The emission cross-section, 1.60×10^{-21} cm^2 at 541 nm for the $Ca_3(VO_4)_2$:$0.05Ho^{3+}$ phosphor, is lower than that of the Ho^{3+}:$NaGd(WO_4)_2$ crystal[62] and Ho^{3+}:$LiYF_4$ (ref. 63) at (2.70 and 8.0) $\times 10^{-21}$ cm^2, respectively. The observed higher branching ratio (83.5%) and the reasonable emission-cross-section for the $^5F_4 + {}^5S_2 \rightarrow {}^5I_8$ transition in the $Ca_3(VO_4)_2$:$0.05Ho^{3+}$ phosphor

Table 2 Doubly reduced matrix elements $\|U^2\|^\lambda$ ($\lambda = 2$, 4 and 6), relative line strengths and Judd–Ofelt intensity parameters for the observed excitation/absorption bands of Ho^{3+} doped $Ca_3(VO_4)_2$:$0.05Ho^{3+}$ phosphor

Transitions	Excitation band wavenumber (ν cm^{-1})	$\|U^2\|^2$	$\|U^2\|^4$	$\|U^2\|^6$	Line strengths ($\times 10^{-20}$ cm^2) S^{ed}_{meas}	S^{ed}_{cal}	Judd–Ofet parameters ($\times 10^{-20}$ cm^2) Ω_2	Ω_4	Ω_6	References
$^5I_8 \rightarrow {}^3H_6 + {}^3H_5$	27 685	0.254	0.2337	0.1609	0.050	0.138	0.16	0.17	0.36	Present work
$^5I_8 \rightarrow {}^5G_4 + {}^3K_7$	25 846	0.0058	0.0361	0.0697	0.050	0.031	0.04	2.67	1.89	YAG[60]
$^5I_8 \rightarrow {}^5G_5$	23 872	0	0.5338	0.0002	0.102	0.088	0.17	2.08	1.92	$Lu_3Al_5O_{12}$ (ref. 59)
$^5I_8 \rightarrow {}^5G_6$	22 020	1.5201	0.8410	0.1535	0.441	0.426	1.16	1.38	0.88	LaF_3 (ref. 61)
$^5I_8 \rightarrow {}^5F_2 + {}^3K_8$	21 186	0.0208	0.0334	0.3576	0.132	0.138	0.41	0.16	0.19	$SrZrO_3$ (ref. 54)
$^5I_8 \rightarrow {}^5F_3$	20 542	0	0	0.3464	0.162	0.125	1.01	1.71	1.21	$LiYF_4$ (ref. 63)
δ_{rms}					±0.161					

Table 3 Relative radiative properties such as spontaneous radiative transition probabilities (A_{rad}), branching ratios (β) and radiative lifetimes, emission cross-sections for the emission transitions of $Ca_3(VO_4)_2$:0.05Ho^{3+} phosphor

Transition	λ (nm)	A_{rad} (S^{-1})	τ_{rad} (μs)	β (%)	σ_{emi} (cm^2)
$^5S_2 + {}^5F_4 \rightarrow {}^5I_8$	541	1000.2	835	83.5	1.6×10^{-21}
$^5F_5 \rightarrow {}^5I_8$	651	447.8	1642	73.5	0.3×10^{-21}

suggest that it is most useful for bright green emitting light for optoelectronic applications.

3.5 Color coordinates and color purity analysis

The emission color and color purity of the synthesized $Ca_3(VO_4)_2$:Ho^{3+} powders were determined by assessing their coordinates on the Commission Internationale de L'Eclairage (CIE) chromaticity diagram. Fig. 9 shows the CIE diagram for all the Ho^{3+}-doped $Ca_3(VO_4)_2$ samples, while Table 4 presents the specific CIE coordinates of $Ca_3(VO_4)_2$:Ho^{3+}, along with the color purity and CCT. It is worth noting that in all cases, the CIE coordinates for these samples consistently fall within the green region. The color purity of the synthesized phosphors is also an important characteristic, and another important parameter that can be calculated by the following formula:[64,65]

$$\text{Color purity}(\%) = \frac{\sqrt{(x - x_i)^2 + (y - y_i)^2}}{\sqrt{(x_d - x_i)^2 + (y_d - y_i)^2}} \times 100 \quad (5)$$

where, (x, y) = sample point coordinates, $(x_d, y_d) = (0.251, 0.737)$ at the dominant wavelength coordinates, and (x_i (0.2815), y_i (0.2971)) are the coordinates of the illuminant point. The color purity values of all the Ho^{3+}-doped samples are also found to be in good agreement at around 67%. The $Ca_3(VO_4)_2$:Ho^{3+} phosphor is suggested as an excellent candidate for use as the green-emitting component in white LED (w-LED) applications. The correlated color temperature (CCT) of the inorganic phosphor can be estimated using eqn (6):[66]

$$\text{CCT} = -437n^3 + 3601n^2 - 6861n + 5514.31 \quad (6)$$

where, with x_e being equal to 0.3320, and y_e being equal to 0.1858.[67] The estimated CCT value for the inorganic phosphors lies in the range (5863–6079) K, which suggests that the phosphor is suitable for a work environment where bright illumination is needed. In w-LEDs, a combination of different phosphors is used to create white light, and having a high-quality green-emitting component is crucial to achieving a balanced and full-spectrum white light output.

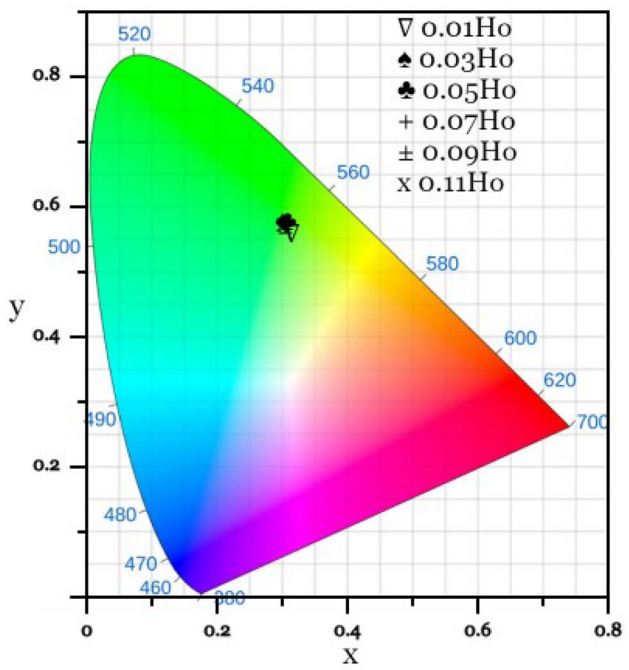

Fig. 9 CIE chromaticity diagram for $Ca_3(VO_4)_2$:Ho^{3+} phosphor.

Table 4 CIE coordinates, color purity and CCT of $Ca_3(VO_4)_2$:xHo^{3+} phosphor

S. no.	Ho^{3+} content (mol)	x	y	Color purity (%)	CCT (K)
1	0.01	0.314	0.557	59.34	5863
2	0.03	0.301	0.578	63.81	6079
3	0.05	0.306	0.577	67.68	5994
4	0.07	0.305	0.576	67.42	6002
5	0.09	0.303	0.570	65.95	6056
6	0.11	0.303	0.574	66.91	6055

4. Conclusion

The investigation of a synthesized phosphor sample, calcium vanadate $Ca_3(VO_4)_2$, doped with varying concentrations of Ho^{3+} ions, has yielded valuable insights into its optical properties and potential applications. The synthesis of these phosphors *via* a sol–gel procedure resulted in well-crystallized powders, ensuring the structural integrity of the material. The discovery of a partial porous structure within the developed phosphors, as revealed by SEM images, adds an intriguing dimension to their potential uses. Under excitation at 451 nm, we observed three emission peaks at around 506 nm ($^5F_3 \rightarrow {}^5I_8$), 545 nm ($^5S_2 + {}^5F_4$) $\rightarrow {}^5I_8$, and 651 nm ($^5F_5 \rightarrow {}^5I_8$). Notably, the study identified a critical dopant concentration (0.05 mol) where quenching of Ho^{3+} emission occurs, likely due to the formation of dopant-ion clusters at higher concentrations. This observation underscores the importance of carefully controlling the dopant levels for optimal performance. The Judd–Ofelt intensity parameters were calculated from the excitation bands, and for Ω_2, Ω_4, and Ω_6 are (0.16, 0.17 and 0.36) $\times 10^{-20}$ cm^2, respectively. Furthermore, evaluation of the CIE chromaticity coordinates allowed for in-depth analysis of the color purity of the $Ca_3(VO_4)_2$:Ho^{3+} phosphor emission. The present investigation on calcium vanadate-based phosphors doped with Ho^{3+} provides valuable insights into their potential use as green light-emitting materials in solid-state lighting technology. The well-

crystallized structures, controllable dopant concentrations, and specific emission properties of these phosphors make them promising for future lighting and display technologies. Further research and practical applications are now possible based on the preliminary results presented.

Conflicts of interest

There are no conflicts to declare.

Acknowledgements

This work was supported by the National Research Foundation of Korea (NRF) grant funded by the Korea government (MSIT) (No. 2021R1A2C1092509). This paper was supported by the KU Research Professor Program of Konkuk University.

References

1 G. B. Nair, H. C. Swart and S. Dhoble, *Prog. Mater. Sci.*, 2020, **109**, 100622–100658.
2 M. D. Mehare, C. M. Mehare, H. C. Swart and S. J. Dhoble, *Prog. Mater. Sci.*, 2022, **133**, 101067–101119.
3 H. Lin, T. Hu, Y. Cheng, M. Chen and Y. Wang, *Laser Photonics Rev.*, 2018, **12**, 1700344–1700375.
4 S. Aralekallu, R. Boddula and V. Singh, *Mater. Des.*, 2023, **225**, 111517–111550.
5 M. H. Fang, Z. Bao, W. T. Huang and R. S. Liu, *Chem. Rev.*, 2022, **122**, 11474–11513.
6 H. Terraschke and C. Wickleder, UV, blue, green, yellow, red, and small: newest developments on Eu^{2+} doped nanophosphors, *Chem. Rev.*, 2015, **115**, 11352–11378.
7 M. Akhtar, G. Anderson, R. Zhao, A. Alruqi, J. E. Mroczkowska, G. Sumanasekera and J. B. Jasinski, *npj 2D Mater. Appl.*, 2017, **1**, 5–18.
8 W. P. Lustig, S. Mukherjee, N. D. Rudd, A. V. Desai, J. Li and S. K. Ghosh, *Chem. Soc. Rev.*, 2017, **46**, 3242–3285.
9 M. Sharma, P. Singh, S. K. Singh and P. Singh, *Opt. Mater.*, 2022, **133**, 112925–112937.
10 L. Wu, P. Dai and D. Wen, *ACS Sustain. Chem. Eng.*, 2022, **10**, 3757–3765.
11 Q. Tang, K. Qiu, W. Zhang, Y. Shen and J. Wang, *Opt. Mater.*, 2018, **75**, 258–267.
12 V. Singh, M. Seshadri, M. S. Pathak and N. Singh, *Spectrochim. Acta, Part A*, 2019, **217**, 315–321.
13 Z. Chen, D. Wang, L. Liu, F. Yuan, Y. Huang, L. Zhang and Z. Lin, *J. Alloys Compd.*, 2023, **938**, 168651–168658.
14 L. Jing, X. Liu, Y. Li and Y. Wang, *J. Lumin.*, 2015, **162**, 185–190.
15 A. K. Bedyal, V. Kumar and H. C. Swart, *J. Alloys Compd.*, 2017, **709**, 362–372.
16 H. M. Yang, J. X. Shi, H. B. Liang and M. L. Gong, *Mater. Res. Bull.*, 2006, **41**, 867–872.
17 L. Sun, J. Yao, C. Liu, C. Liao and C. Yan, *J. Lumin.*, 2000, **87**, 447–450.
18 X. Huang, B. Li and H. Guo, *J. Alloys Compd.*, 2017, **695**, 2773–2780.
19 B. G. Zhai and Y. M. Huang, *J. Mater. Sci.*, 2017, **52**, 1813–1822.
20 G. M. Kuz'micheva, L. I. Ivleva, I. A. Kaurova, E. V. Khuramov, V. B. Rybakov and M. E. Doroshenko, *J. Alloys Compd.*, 2021, **854**, 155918–155928.
21 I. S. Voronina, V. V. Voronov, E. E. Dunaeva, L. D. Iskhakova, A. G. Papashvili, M. E. Doroshenko and L. I. Ivleva, *J. Cryst. Growth*, 2021, **555**, 125965–125972.
22 G. M. Kuz'micheva, L. I. Ivleva, I. A. Kaurova, E. V. Khramov, V. B. Rybakov and M. E. Doroshenko, *Mater. Res. Bull.*, 2021, **140**, 111300–111311.
23 L. I. Ivleva, E. E. Dunaeva, I. S. Voronina, M. E. Doroshenko, A. G. Papashvili, J. Sulc, J. Kratochvíl and H. Jelinkova, *J. Cryst. Growth*, 2019, **513**, 10–14.
24 K. Qiu, J. Li, J. Li, X. Lu, Y. Gong and J. Li, *J. Mater. Sci.*, 2010, **45**, 5456–5462.
25 H. Y. Lin, W. F. Chang and S. Y. Chu, *J. Lumin.*, 2013, **133**, 194–199.
26 A. A. Bhat, S. A. Khandy, A. M. Ali and R. Tomar, *J. Phys. Chem. Lett.*, 2023, **14**, 5004–5012.
27 A. A. Bhat and R. Tomar, *J. Alloys Compd.*, 2021, **876**, 160043–160052.
28 H. Zhang, M. Lü, Z. Xiu, S. Wang, G. Zhou, Y. Zhou, S. Wang, Z. Qiu and A. Zhang, *Mater. Res. Bull.*, 2007, **42**, 1145–1152.
29 V. Singh, S. Kaur and M. Jayasimhadri, *Solid State Sci.*, 2020, **101**, 106049–106054.
30 V. Singh, S. Kaur, C. B. A. Devi, A. S. Rao and J. B. Joo, *Optik*, 2022, **266**, 169553–169562.
31 J. K. Lee, A. Nande, A. A. Bhat, S. Watanabe, T. G. Rao and V. Singh, *Ceram. Int.*, 2024, **50**, 17063–17074.
32 V. Chauhan, P. K. Pandey, P. Dixit and P. C. Pandey, *Mater. Today: Proc.*, 2022, **67**, 605–608.
33 L. Li, Y. Pan, W. Wang, W. Zhang, Z. Wen, X. Leng and X. Liu, *J. Alloys Compd.*, 2017, **726**, 121–131.
34 A. A. Bhat, S. A. Khandy, I. Islam and R. Tomar, *Sci. Rep.*, 2021, **11**, 16473–16485.
35 V. Rajalingam, Synthesis and Characterization of BiVO4 nanostructured materials: application to photocatalysis, Doctoral dissertation, Université du Maine, 2014.
36 M. A. Zaitoun, D. M. Goken, L. S. Bailey, T. Kim and C. T. Lin, *J. Phys. Chem. B*, 2000, **104**, 189–196.
37 K. Nakanishi, R. Takahashi, T. Nagakane, K. Kitayama, N. Koheiya, H. Shikata and N. Soga, *J. Sol-Gel Sci. Technol.*, 2000, **17**, 191–210.
38 G. S. Grader, Y. De Hazan, D. Bravo-Zhivotovskii and G. E. Shter, *J. Sol-Gel Sci. Technol.*, 1997, **10**, 127–137.
39 N. Job, A. Théry, R. Pirard, J. Marien, L. Kocon, J. N. Rouzaud, F. Béguin and J. P. Pirard, *Carbon*, 2005, **43**, 2481–2494.
40 V. Singh, G. Lakshminarayana, A. Wagh and N. Singh, *Optik*, 2020, **207**, 164284–164290.
41 C. S. Rao, K. U. Kumar, P. Babu and C. K. Jayasankar, *Opt. Mater.*, 2012, **35**, 102–107.
42 V. Singh, N. Singh, M. S. Pathak, P. K. Singh and V. Natarajan, *Optik*, 2018, **171**, 356–362.
43 A. A. Bhat, N. Singh, R. V. Nair, E. Dujardin and J. Sharma, *Opt. Mater.*, 2023, **141**, 113937–113943.

44 S. Babu, M. Seshadri, A. Balakrishna, V. R. Prasad and Y. C. Ratnakaram, *Phys. Rev. B: Condens. Matter Mater. Phys.*, 2015, **479**, 26–34.
45 A. Dwivedi, A. K. Singh and S. B. Rai, *Dalton Trans.*, 2014, **43**, 15906–15914.
46 T. Li, C. Guo, H. Suo and P. Zhao, *J. Mater. Chem. C*, 2016, **4**, 1964–1971.
47 A. Li, R. Lu, Y. Zhao, J. Yang, J. Wang and G. Zhao, *J. Lumin.*, 2022, **248**, 118962–118967.
48 D. K. Sardar, S. R. Chandrasekharan, K. L. Nash, J. B. Gruber, A. Burger and U. N. Roy, *J. Appl. Phys.*, 2008, **103**, 093112–093120.
49 G. Blasse, *J. Electrochem. Soc.*, 1968, **115**, 738–742.
50 D. L. Dexter and J. H. Schulman, *J. Chem. Phys.*, 1954, **22**, 1063–1070.
51 W. Luo, J. Liao, R. Li and X. Chen, *Phys. Chem. Chem. Phys.*, 2010, **12**, 3276–3282.
52 S. Dutta, S. Som and S. K. Sharma, *RSC Adv.*, 2015, **5**, 7380–7387.
53 V. Singh, M. Seshadri, D. Taikar, S. J. Dhoble and R. S. Yadav, *RSC Adv.*, 2023, **13**, 3592–3601.
54 V. Singh and M. Seshadri, *RSC Adv.*, 2023, **13**, 27782–27791.
55 B. R. Judd, *Phys. Rev.*, 1962, **127**, 750–761.
56 G. S. Ofelt, *J. Chem. Phys.*, 1962, **37**, 511–520.
57 R. D. Peacock, *Struct. Bonding*, 1975, **22**, 83–122.
58 E. W. J. L. Oomen and A. M. A. van Dongen, *J. Non-Cryst. Solids*, 1989, **111**, 205–213.
59 D. N. Patel, B. R. Reddy and S. K. Nash-Stevenson, *Opt. Mater.*, 1998, **10**, 225–234.
60 M. Malinowski, Z. Frukacz, M. Szuflinskaa, A. Wnuk and M. Kaczkan, *J. Alloys Compd.*, 2000, **300**, 389–394.
61 M. J. Weber, B. H. Matsinger, V. L. Dolan and G. Surratt, *J. Chem. Phys.*, 1972, **57**, 562.
62 H. Wang, J. Li, G. Jia, Z. You, F. Yang, Y. Wei, Y. Wang, Z. Zhu, X. Lu and C. Tu, *J. Alloys Compd.*, 2007, **431**, 277–281.
63 B. M. Walsh, G. W. Grew and N. P. Barnes, *J. Phys.: Condens.Matter*, 2005, **17**, 7643–7665.
64 A. A. Bhat, I. Assadullah, A. Farooq, K. A. Malik, J. H. Malik, R. Tomar, I. Islam, A. M. Ali and S. A. Khandy, *Mater. Chem. Phys.*, 2023, **306**, 127993–128000.
65 M. Seshadri, L. C. Barbosa and M. Radha, *J. Non-Cryst. Solids*, 2014, **406**, 62–72.
66 L. Wang, S. Jilili, A. Tuerxun, A. Sidike and Q. Wang, *Jpn. J. Appl. Phys.*, 2022, **61**, 062002–062009.
67 Y. Li, J. Chen and C. Chen, *Optik*, 2018, **174**, 1–6.